PHYSICS

All twist and no bend makes raft edges splay: Spontaneous curvature of domain edges in colloidal membranes

Joia M. Miller[1,2]*, Doug Hall[3], Joanna Robaszewski[1,2], Prerna Sharma[4], Michael F. Hagan[1], Gregory M. Grason[3†], Zvonimir Dogic[1,2†]

Using theory and experiments, we study the interface between two immiscible domains in a colloidal membrane composed of rigid rods of different lengths. Geometric considerations of rigid rod packing imply that a domain of sufficiently short rods in a background membrane of long rods is more susceptible to twist than the inverse structure, a long-rod domain in a short-rod membrane. The midplane tilt at the interdomain edge forces splay, which, in turn, manifests as spontaneous edge curvature with energetics controlled by the length asymmetry of constituent rods. A thermodynamic model of such tilt-curvature coupling at interdomain edges explains a number of experimental observations, including annularly shaped long-rod domains, and a nonmonotonic dependence of edge twist on domain radius. Our work shows how coupling between orientational and compositional degrees of freedom in two-dimensional fluids gives rise to complex shapes of fluid domains, analogous to shape transitions in 3D fluid vesicles.

INTRODUCTION

A membrane's local composition is geometrically coupled to its structure. As such, inclusions and domains of different composition deform the background membrane structure, and this deformation in turn generates interactions and instabilities that have no analogs in three-dimensional (3D) isotropic solvents (*1*–*3*). For example, domains can change the locally preferred membrane thickness or curvature, leading to deformations that propagate into the membrane interior and generate effective long-ranged interactions (*4*). In particular, two component membranes exhibit a pronounced tendency to demix into distinct domains separated by a 1D interdomain edge (*5*–*7*). In biology, such phase-separated finite-sized domains, called lipid rafts, acquire important functional roles (*8*–*10*). In synthetic monolayers and bilayer membranes, phase-separated domains are ubiquitous and can assume intriguing noncircular shapes (*11*–*13*). Notwithstanding substantial progress in studying various aspects of membrane-like materials, the interplay between orientational and compositional order in multicomponent fluid membranes and its effect on domain size, morphologies, and thermodynamics remains poorly understood.

Colloidal membranes are one rod–length–thick, liquid-like monolayers that spontaneously assemble from a mixture of monodisperse colloidal rod-like particles and nonadsorbing polymers (*14*–*16*). They are micrometer-sized analogs of conventional lipid bilayers that provide the unique opportunity to visualize and quantify intramembrane domain structures and to elucidate the fundamental principles that underlie their behaviors. Previous work showed that, when dissolved in a colloidal membrane, rods of a different length robustly assemble into raft-like domains, which are finite-sized liquid-like droplets (*17*–*19*). We study the structure of interdomain edges of such colloidal rafts, showing that geometric frustration between double-twist and splay of rigid-rod rafts leads to spontaneous nonzero edge curvature toward the shorter-rod domain. A theoretical model that captures the coupling between rod orientation and the interface edge-curvature explains the experimental observations, including (i) enhancement or suppression of edge tilt for the short-rod and long-rod rafts, respectively, (ii) a nonmonotonic dependence of the edge twist on the edge curvature, and (iii) the shape instability of the circular long-rod rafts, which above a critical size spontaneously transform into annular liquid droplets.

These results have broad implications. It is known that certain gradient patterns of liquid crystal orientations are mutually incompatible (*20*). For example, bending of a 3D nematic without splay necessarily requires twist, this being the origin of the "twist-bend" phases. Analogously, adopting a "double-twisted" texture without bend (i.e., "all twist and no bend") necessarily introduces asymmetric splay at domain interfaces, a manifestation of the recently described "splay-twist" texture (*21*). Furthermore, our findings demonstrate a chirality-independent mechanism that drives spontaneous interfacial twist in membranes composed of rods with sufficiently different lengths. This mechanism could stabilize assembly of finite-sized colloidal rafts even in weakly chiral or achiral systems (*22*). More generally, these results show that the interplay between orientation and composition in phase-separated membranes gives rise to shape selection mechanisms for nonconvex 2D "droplets" that are reminiscent of those studied in 3D vesicles (*23*).

RESULTS

Geometry of length-asymmetric rod domains

We consider a phase-separated membrane composed of rigid, rod-like particles with two different lengths, $\ell_{in} \neq \ell_{out}$. We assume that all rods have smectic-like order with their centers confined to the 2D midplane. The phase separation occurs by formation of a circular raft of radius R composed of rods of length ℓ_{in}, surrounded by a background membrane composed of the alternate length rods, ℓ_{out}. The local

[1]Department of Physics, Brandeis University, Waltham, MA 02454, USA. [2]Department of Physics, University of California, Santa Barbara, Santa Barbara, CA 93106, USA. [3]Department of Polymer Science and Engineering, University of Massachusetts, Amherst, MA 01003, USA. [4]Department of Physics, Indian Institute of Science, Bangalore 560 012, India.
*Present address: Department of Physics, Georgetown University, Washington, DC 20047, USA.
†Corresponding author. Email: grason@mail.pse.umass.edu (G.M.G); zdogic@ucsb.edu (Z.D.)

rod alignment is described by an axisymmetric double-twist whirlpool-like pattern of tilt (Fig. 1, A to D). In polar coordinates, the director field around the raft center can be specified in terms of the midplane position (r_0, ϕ) of the rod centers as $\mathbf{n}(r_0, \phi) = \cos\theta(r_0)\ \hat{z} + \sin\theta(r_0)\ \hat{\phi}$, where $\theta(r_0)$ is the tilt angle relative to the membrane normal, $\hat{z}$. We consider profiles where the director aligns with the membrane normal at the raft center $[\theta(0) = 0]$, twists to a finite value at the raft edge $[\theta(r_0 = R) = \theta_0]$, and then unwinds back to the membrane normal far away from the raft $[\theta(r_0 \to \infty) = 0]$. Previous models have shown that such a director pattern can be driven by asymmetric preferences for cholesteric twist in the distinct domains (*17*, *18*). Here, we describe a chirality-independent mechanism in which the asymmetry between two rod lengths renders the domain interface susceptible to tilt at curved edge, deriving purely from geometric frustration between twist, splay, and bend in rafts.

The radial twist pattern leads to a generic coupling between rod twist and local density (Fig. 1B). When the rod's persistence length is larger than the its contour length, bend is expelled from the raft, and the rod trajectories at radial position, r_0, can be described by $\mathbf{r}(r_0, \phi, z_0) = r_0\hat{r} + z_0\mathbf{n}$, where $z_0 \in [-\ell/2, \ell/2]$ is the arc length along the rod relative to the midplane. Hence, surfaces of fixed r_0 are ruled surfaces, spanned by a set of straight lines (i.e., the rod trajectories) that maintain constant tilt $\theta(r_0)$ (Fig. 1B). The radial distance of rods from the raft center is $r_\perp(r_0, z) = \sqrt{r_0^2 + z^2\tan^2\theta_0}$, where $z = z_0\cos\theta_0$ is the raft vertical height. Consequently, rods at fixed r_0 lie in a hyperboloid, implying that the raft geometry can be decomposed into nested hyperboloids whose geometry is specified by r_0 and θ_0.

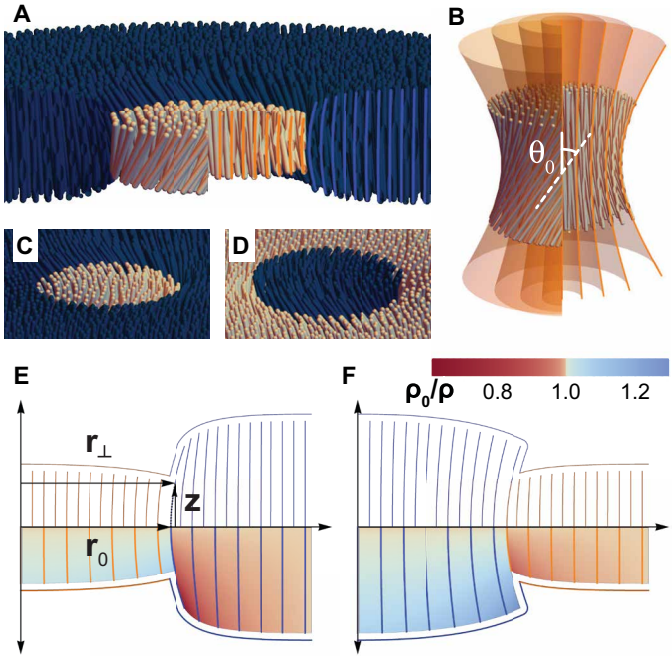

Fig. 1. Twist-splay coupling in colloidal rafts. (**A**) A twisted raft within a background membrane of longer rods. (**B**) Hyperbolic structure of a raft composed of twisted rigid rods. Rods passing through the midplane at the same radial distance from the center define a hyperboloid surface. θ_0 is the angle of maximum tilt with respect to vertical. (**C** and **D**) Rafts are composed of short and longer rods, respectively. (**E**) Twist induces dilation of the short rods within the raft and compression of the long rods in the outer membrane, decreasing the total membrane volume that is inaccessible to depletants. Color indicates normalized local density ranging from low (blue) to high (red). (**F**) Long-rod rafts have dilation of the long rods and compression of the short rods, leading to a net increase in the excluded volume and unfavorable structures.

Splayed liquid crystalline configurations, where $\nabla \cdot \mathbf{n} \neq 0$, are costly because they introduce variation away from the preferred interrod (areal) density ρ. This follows from the "conservation law": $(\mathbf{n} \cdot \nabla)\rho = -\rho(\nabla \cdot \mathbf{n})$, which holds for membranes in which rod ends are expelled to the top and bottom boundary (*24*, *25*). Along the midplane $(z_0 = 0)$, the raft director field is given by the splay-free double twist pattern $\mathbf{n}(r_0, \phi)$. However, the combination of zero bend and variable tilt introduces splay away from the midplane, forcing rods to deviate from constant spacing (*26*). Graphically, this can be seen from the "frayed" geometry of the nested hyperboloids as the rods tilt away from $\hat{z}$ (Fig. 1B). Mathematically, this splay is related to radial tilting of the hyperboloids $\frac{\partial r_\perp}{\partial z} \cong z\tan^2\theta(r_\perp)/r_\perp$, where $r_\perp \cong r_0$, and we consider small z for simplicity. Because rods live on these surfaces, the radial component of the director is $\frac{\partial r_\perp}{\partial z}$. Near the midsurface $\nabla \cdot \mathbf{n} = r^{-1}\partial_r(r\, n_r) \propto z\,\partial_r(\tan^2\theta)/r$ (section S2 and eq. S12). Consequently, splay arises away from the membrane midplane due to the radial gradients of tilt. In turn, the conservation law implies that with increasing splay, the rod density ρ drops away from the midplane. This local density expansion is maximal at the top and the bottom of the inner raft edge. Furthermore, a decreasing tilt profile in the outer membrane, where rods tilt back toward the membrane normal, generates compression, with the local density being highest at the rod ends (Fig. 1, E and F). The expansion and compression of the inner and outer raft edges are consequences of the variable double-twist texture.

The splay-twist coupling has a profound effect on the structure and thermodynamics of the domain interface that has not been considered previously (*17*, *18*). We first consider a model of colloidal monolayers of chiral rod-like molecules that are condensed by the depletant polymers. Entropy favors the maximal volume accessible to the depletants, which occurs for membrane configurations that minimize volume because the membrane is inaccessible to the depletant (*16*). A straight, zero-curvature interface between long and short rods would have a square-like cross-sectional profile, and rod tilt parallel to the interface would not introduce splay (Fig. 2, C and D, and movie S1). Curving such a twisted interface toward short rods produces a double-twisted director field upon tilting of the rods. In turn, the geometric argument outlined above illustrates that this causes volume expansion of the inner short-rod portion of the edge, but this is more than compensated by the larger decrease in accessible volume in the compressed outer long-rod portion of the interface. Overall the curved interface reduces the net volume excluded to the polymer and is, thus, energetically favorable when compared with the straight interface (Fig. 2, A and B). Analogously, curving the twisted interface toward the long-rod rafts will increase the net membrane volume because the expansion of the long-rod raft is larger than the complementary compression of the short rods (Fig. 2, E and F). We argue that the asymmetric expansion/compression favors interface curvature toward the shorter-rod domains and away from the longer-rod domains and drastically increases the susceptibility of so-curved interfaces to edge twist.

Edge tilt dependence on raft size

To test these ideas, we used colloidal membranes, which are one rod–length–thick liquid-like monolayers of aligned rods assembled

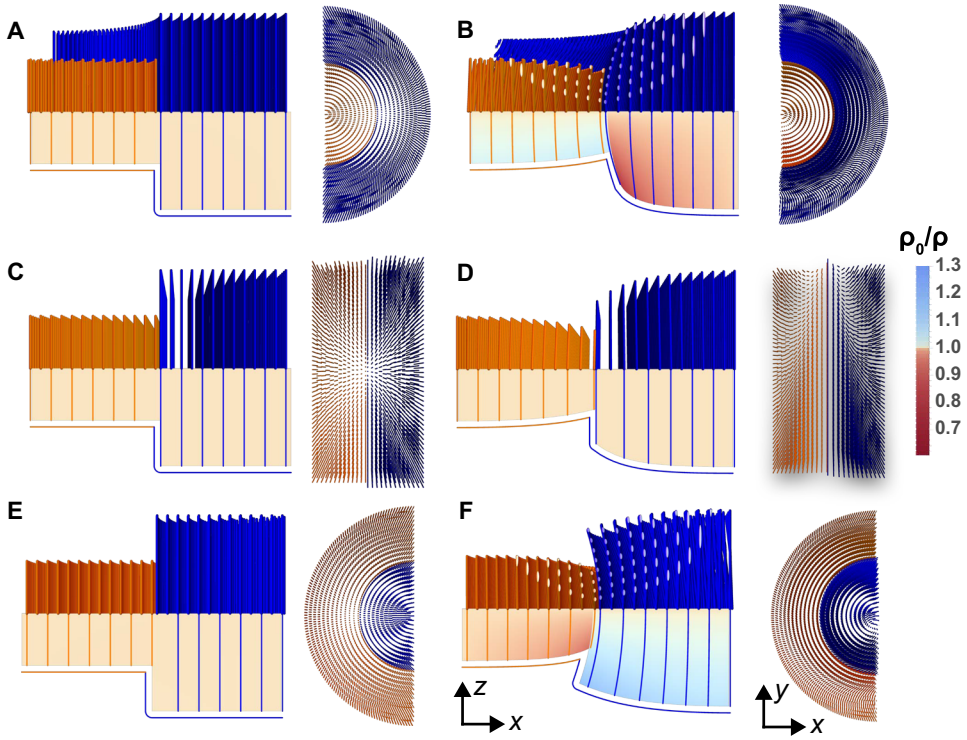

Fig. 2. Coupling between interface curvature, rod tilt, and density. (**A** and **B**) Structure of domain interface with curvature toward short rods ($\kappa_g < 0$). Left: Side and top views show the constant rod density of an untwisted curved domain. Right: The same interface with rod twist shows a splayed structure and expansion of the short rods and compression of the long rods. (**C** and **D**) For interface without spontaneous curvature ($\kappa_g = 0$), the rod density is constant whether rods are straight or tilted. (**E** and **F**) When $\kappa_g > 0$, rod density around the untwisted interface again remains constant, while rod twist leads to expansion of the long and compression of the short rods.

by the depletion interaction (*14*–*16*). Previous work showed that 880-nm-long left-handed *fd*-Y21M rod–like viruses formed finite-sized colloidal rafts when dissolved in a background membrane composed of 1200-nm-long M13KO7 rods of the opposite chirality (*19*). The structure of these rafts is revealed by LC-PolScope, an imaging technique that quantitatively measures local retardance. When constituent rods are parallel to the normal of the membrane that lies in the image plane, the LC-PolScope retardance image is near zero. Rod tilt away from the membrane normal introduces local birefringence, which leads to increased signal in LC-PolScope images (*27*, *28*). Imaging short-rod *fd*-Y21M rafts with LC-PolScope revealed a bright ring around the raft edges, which is indicative of local tilt (Fig. 3, A and C, and movies S2 and S3). We explored the complementary regime, in which a low volume fraction of M13KO7 long rods was dissolved in a membrane of short *fd*-Y21M rods. The long rods also formed finite-sized clusters, but these were more heterogeneous (Fig. 3B and movie S2). Observing such clusters with LC-PolScope revealed the absence of any measurable twist of similarly sized rafts (Fig. 3, D and E). Theories that consider only the effect of chiral asymmetry between the raft and the background domain predict that equal-sized rafts of both short and long rods would twist by the same amount. In contrast, the near-complete suppression of the edge twist in the long-rod rafts in the presence of chiral asymmetry implies that the interface structure is sensitive to the length difference between the inner and the outer phase, consistent with previously outlined geometrical arguments.

To quantify these effects, we extended the existing smectic-layer model of chiral colloidal rafts (*16*, *17*) by incorporating the thermodynamic costs due to the hyperbolic edge geometry (section S1). In the smectic model, phase-separated domains are described by Frank elastic gradients for bend, splay, and twist along the midplane (*29*). We assume that all elastic deformations have the same elastic constant K. The chiral preferences of the inner and outer domains are parameterized by the inverse pitch parameters q_{in} and q_{out}. Our model also includes a penalty for rod tilt away from the layer normal that derives from the osmotic cost (Π per unit volume) of increasing areal exposure of a depletion layer of thickness a at the top and bottom surface upon tilt while maintaining a constant interrod density at the midplane. The thickness of this layer is determined by a, a radius of gyration of depleting polymers. A torque balance between the two effects gives equilibrium profiles of tilt that extend from the interdomain edge by a penetration length $\lambda = \sqrt{K\ell/2\Pi a}$. Our model accounts for the changes in the excluded volume due to the compression/dilation of the hyperbolic domain edge. As discussed above, splay deformation requires variation of the interrod density ρ in the layer away from the preferred value. We approximate this cost by a two-body term $A_2\rho^2/2$, where A_2 is the second virial coefficient for interrod density. In combination with the rod translational entropy, this balances the osmotic pressure exerted by the enveloping depletant.

Our central result is summarized by considering an expansion of the raft free energy for radius R in terms of the maximum interface tilt θ_0

$$F(\theta_0, R) = 2\pi R\gamma + 2\pi R\,\theta_0\,K\Delta(q\ell) + \frac{\chi^{-1}(R)}{2}\theta_0^2 + O(\theta_0^4) \qquad (1)$$

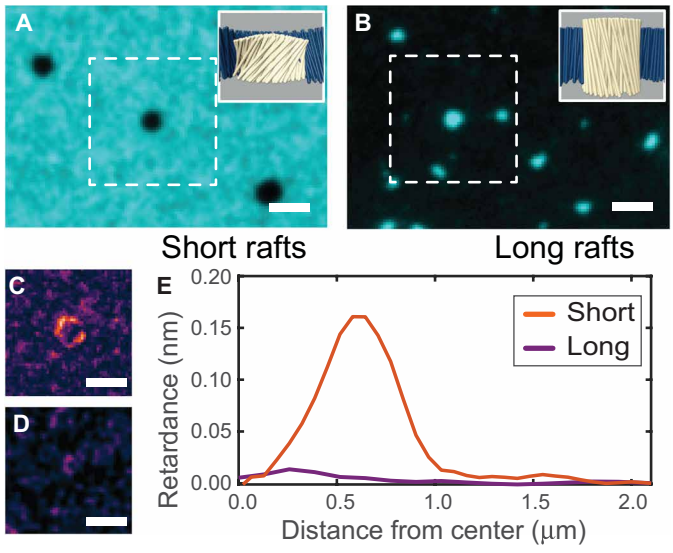

Fig. 3. Structure of short- and long-rod rafts. (**A**) Chiral short-rod rafts in a long-rod membrane of opposite chirality. Long rods are fluorescently labeled. Inset: Schematic of raft structure. (**B**) Rafts composed of fluorescently labeled long rods in a short-rod background membrane. (**C**) An LC-PolScope image highlights the tilt localized at the edge of the short-rod raft. Image intensity corresponds to the magnitude of the local tilt. (**D**) An LC-PolScope image of a comparable long-rod raft shows no measurable tilt. (**E**) Radially averaged retardance, which is proportional to the edge tilt, for the short- and long-rod rafts. Scale bars, 2 μm.

Here, $\gamma = \Pi a \mid \ell_{in} - \ell_{out} \mid$ is the tilt-independent line tension due to depletion at the "side wall" between the long and short domains. The next term represents the linear free energy gain due to twist in opposing sides of domain edge, which is proportional to the difference between the preferred inverse pitch of raft and membrane domains for the case of length-symmetric rods (*16*, *17*) but, more generally, depends on the difference of the product of rod length and chirality $\Delta(q\ell) = q_{out}\ell_{out} - q_{in}\ell_{in}$. The second-order coefficient, $\chi^{-1}(R) = \chi^{-1}_{sm}(R) + \chi^{-1}_{edge}(R)$, describes the tilt stiffness, or inverse tilt susceptibility, and has two contributions. The previously derived smectic contribution $\chi^{-1}_{sm}(R)$ arises from the balance of elastic costs of tilt gradients and the penalty for tilt (*17*). For small rafts, the linear gradient of tilt within the raft generates a constant stiffness $\chi^{-1}_{sm}(R \ll \lambda) \approx K\ell$, while for large rafts, the localized tilt at the edge gives rise to a tilt stiffness $\chi^{-1}_{sm}(R \gg \lambda) \approx K\ell R/\lambda$. The second contribution to the tilt stiffness, $\chi^{-1}_{edge}(R)$, arises from the hyperbolic geometry of the raft/membrane edge

$$\chi^{-1}_{edge}(R) = \alpha\Pi\,\partial^2_{\theta_0} V_{edge} + a\Pi\,\partial^2_{\theta_0} A_{edge} \quad (2)$$

Here, V_{edge} and A_{edge} are contributions from the volume and surface area change of the membrane due to the hyperbolic raft edge shape (eqs. S15 and S16). The coefficient α derives from the net work of osmotic pressure in the change in edge volume and counterbalancing change in two-body rod-rod interactions due to the splay-induced compression/dilation. We estimate a value of $\alpha = \rho\frac{k_B T}{\Pi\ell} < 1$, which can be expected based on the van't Hoff law prediction for experimentally relevant osmotic pressures. Expansion to the lowest order in the tilt angle yields $V_{edge} \simeq \pi(\ell^3_{in} - \ell^3_{out})\theta_0^2/12$ and $A_{edge} \simeq \pi \mid \ell^3_{in} - \ell^3_{out} \mid \theta_0^2/(12\ R) + \pi(\ell^2_{in} - \ell^2_{out})\theta_0^2/2 - \pi \mid \ell_{in} - \ell_{out} \mid R\,\theta_0^2$. The volume change results from the difference between the compression/expansion of the inner and outer membrane edge, while the area change results from the corresponding change in the hyperbolic edge surface area. For short-rod rafts $V_{edge}(\ell_{in} < \ell_{out}) < 0$, indicating that the osmotic pressure of the enveloping polymer increases the tilt susceptibility, whereas for long-rod rafts ($\ell_{in} > \ell_{out}$), the net dilation of the membrane volume stiffens the resistance to tilt. Note that the length asymmetry of the tilt susceptibility is further enhanced by a factor proportional to $a(\ell^2_{in} - \ell^2_{out})$ deriving from the change of $A_{edge}(\ell_{in} < \ell_{out})$. Because $\chi(R) \mid_{\ell_{in} < \ell_{out}} > \chi(R) \mid_{\ell_{in} > \ell_{out}}$, the equilibrium tilt at a given raft size, $\theta^*(R) = 2\pi R\, K\Delta(q\ell)\,\chi(R)$, increases with length asymmetry of small-rod rafts and is suppressed for the long-rod rafts. The latter prediction is consistent with the observed suppression of twist of long-rod rafts (Fig. 3, D and E).

Another central prediction of our model is the nonmonotonic dependence of the maximum edge twist $\theta(R)$ of short-rod rafts as a function of raft radius R. With increasing size, the maximum angle $\theta_0(R)$ first increases, reaching a maximum for raft sizes that are of the order of the twist penetration length. Increasing the raft size further untwists the interface (Fig. 4B). This behavior derives from the generic evolution of twist stiffness $\chi^{-1}(R)$ with raft size. In the $R \to 0$ limit, the hyperbolic edge geometry stiffens rafts with $A_{edge} \to \pi \mid \ell^3_{in} - \ell^3_{out} \mid \theta_0^2/(12\ R)$ (Fig. 4A, left); at intermediate sizes, the net compression of the V_{edge} leads to a softened response to twist (Fig. 4A, middle), while for large rafts, the hyperbolic geometry of twisted edges is flattened and the linear growth of $\chi^{-1}_{sm}(R \gg \lambda) \approx K\ell R/\lambda$ dominates, restiffening the raft to twist (Fig. 4A, right). The model predicts that the rod-length difference strongly influences the nonmonotonic dependence of twist on raft size, with a peak in maximum twist occurring when the length difference is comparable to the experimental values (Fig. 4B). In comparison, the predicted twist for rafts as radius $R \to \infty$ is independent of $\Delta\ell$.

To test this prediction, we measured the maximum twist for different-sized short-rod rafts using LC-PolScope. With increasing radius, the retardance increased, reaching a maximum for ~1.5-μm-diameter rafts (Fig. 4, D and E). Beyond this, size maximum retardance decreased, eventually dropping to near background levels (Fig. 4F). To clarify the contribution of chiral effects, we repeated measurements for background membranes with different chirality strengths by mixing different ratios of left-handed (M13KO7) and right-handed (M13KO7-Y21M) (*22*, *30*). Using this method, the background membranes were tuned to be either strongly left-handed ($\phi_{BG} = 1.0$) compared with the above weakly chiral membranes ($\phi_{BG} = 0.4$), or effectively achiral ($\phi_{BG} = 0$) (Fig. 4C). All three cases exhibited nonmonotonic behaviors, but the peak in the twist for the fully chiral background was substantially less pronounced.

Long-rod raft shape instability

It is illuminating to recast the thermodynamic coupling between the double-twist and edge curvature in terms of an effective line energy for the edge length s and its geodesic curvature κ_g. In the limit of large and slowly varying edge curvature, this takes the following form

$$E_{edge} \cong \oint ds \left[\gamma' + \frac{B}{2}(\kappa_g - \kappa_0)^2\right] \quad (3)$$

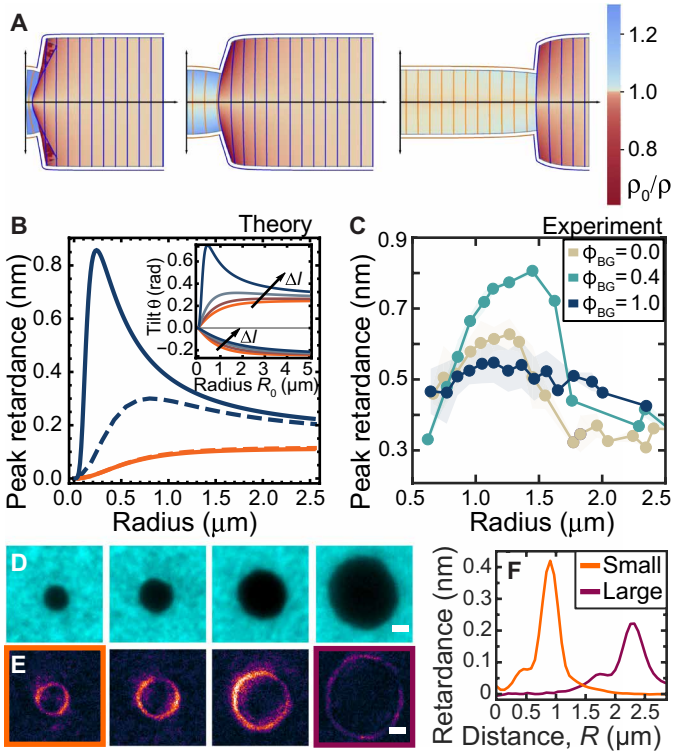

Fig. 4. Nonmonotonic dependence of the edge twist on the raft size. (**A**) Local membrane density maps with maximum raft twist held constant for three different raft radii, $r = 0.15$, 1.0, and 1.8 μm and $\Delta l = 0.86$ μm, illustrating the geometric origin of a nonmonotonic stiffening/softening resistance to edge twist with size. (**B**) Predicted maximum retardance for $\Delta l = 0$ (orange line) and $\Delta l = 0.26$ μm (blue line). Solid lines represent linear model predictions, while dashed lines represent predictions of the full nonlinear calculation. Inset: Predicted maximum raft tilt for length differences of $\Delta l = \pm 0.1$, 0.2, 0.26 μm. Increasing Δl leads to a pronounced peak in the maximum retardance as a function of raft radius, while negative values of Δl predict the suppression of edge twist for long-rod rafts. (**C**) Experimental edge retardance plotted as a function of raft radius demonstrates nonmonotonic dependence of twist on the raft size. Plots are for short-rod rafts dissolved in background membranes with three different chiralities. $\phi_{BG} = 0$ (37% M13KO7, 63% M13KO7-Y21M) indicates an achiral background membrane, while $\phi_{BG} = 1.0$ (100% M13KO7) indicates the strongest left-handed chirality. (**D** and **E**) Fluorescence and LC-PolScope images of rafts of increasing sizes highlighting the nonmonotonic retardance magnitude with increasing radius. Scale bars, 1 μm. (**F**) Radially averaged retardance for the smallest and largest rafts shown in (B).

where $\gamma' \cong \gamma - \delta\gamma^*$ is the line tension renormalized by chiral edge twist, $\delta\gamma^* \approx K\ell\lambda^2(\Delta q)^2$ (section S2). The hyperbolic edge geometry generates an effective edge bending elasticity for length asymmetric membranes, with bending stiffness $B \cong K\ell(\Delta q)^2 \mid \ell_{in}^3 - \ell_{out}^3 \mid$, and a preferred geodesic curvature $\kappa_0 = \mathrm{sgn}(\ell_{out} - \ell_{in})\left(\frac{\alpha}{2a} + \frac{3}{|\ell_{in} - \ell_{out}|}\right)$, reflecting the preference for twisted edges to bend toward the short-rod domain, as is observed in short-rod rafts. Considering the opposite scenario of long-rod rafts, the preferred edge curvature, κ_0, resists the generic tendency to maintain a circular shape, favored by positive γ'. Furthermore, it suggests that circular long-rod rafts will become unstable to nonconvex, and ultimately topologically nontrivial, domain shapes.

Long-rod rafts exhibited such marked shape instabilities with increasing area. In native samples, most long-rod rafts were disk shaped with area ~1 μm^2. Intriguingly, the occasionally observed larger rafts always assumed anisotropic shapes. To quantify this instability, we systematically increased the size of long-rod rafts. Weak repulsive interactions allowed us to merge long-rod rafts with optical tweezers, thus systematically increasing their size (Fig. 5B). After reaching an area of ~1.5 μm^2, such rafts assumed elongated shapes (Fig. 5A). Above a ~4-μm^2 critical area, they transformed into nonconvex horseshoe-like shapes, reminiscent of stomatocyte vesicle shapes (movie S4) (*23*). Further size increase yielded closed and stable annularly shaped rafts, where short rods resided both inside and outside the long-rod raft with annular shape. The evolution of raft shapes was quantified by plotting the ratio of the minor to major axis of the structure. The marked decrease in the ratio indicated a transition from a circular disk to an elongated shape (Fig. 5C). The subsequent increase and the plateau signified the transition to horseshoe-like structures and closed annuli.

To describe annulus formation, we adapted the circular raft model to an annular geometry with variable inner/outer radii and tilt angles (section S3). Plotting the relative free energy of a compact long-rod raft and an annular domain with a twisted, short-rod raft at its center shows that increasing the total area of long-rod rafts reduces the effect of tilt-mediated edge-edge repulsions in the annular domain by increasing the separation between the inner and outer edges (Fig. 5E). For sufficiently large area, the incorporation of an inner edge with the preferred direction of the geodesic curvature outweighs the low edge-edge repulsion to stabilize annuli over disks (Fig. 5D).

The model of annular rafts assumed a twisted inner interface, which was not apparent in our initial fluorescence experiments. In comparison, LC-PolScope revealed clear differences in the structures of the inner and outer interfaces of the annular rafts. Rods are twisted along the inner edge, and this twist was comparable in magnitude to that of a similarly sized short-rod raft in a long-rod background (Fig. 6, A and B). In contrast, the outer edge retardance was only slightly above the background level, indicating the absence of measurable twist at the outer long-rod–to–short-rod interface, much like the retardance measurements for long-rod rafts (Figures 3E and 6E). These structural findings agree with the model, which predicts a strongly twisted inner and a weakly twisted outer interface (Fig. 6, C and D). Such twist asymmetry yields different fluctuations of the inner and outer interface (movie S5). Analogous to the free edge of a membrane (*31*, *32*), the twist of the inner annular interface introduces an elastic penalty that suppresses small wavelength fluctuations. In comparison, the outer untwisted interface has no such penalty and exhibits enhanced fluctuations.

DISCUSSION

Using a combination of experiments and theory, we have described a generic geometric coupling between the orientation and composition of phase-separated fluid membranes. We demonstrated that the length asymmetry of the constituent rods gives rise to a previously unknown mechanism of domain shape selection that is driven by a spontaneous nonzero curvature of the interface toward the shorter-rod domain. The consequences of spontaneous curvature have been extensively studied for analogous 3D vesicles, where locally selected edge curvature generated by the asymmetry in the two bilayer leaflets drives large-scale shape changes (*23*, *33*). Membrane-embedded fluid rafts are similar to 3D vesicles in that they can assume multiple polymorphic shapes. However, there are also differences. For 2D

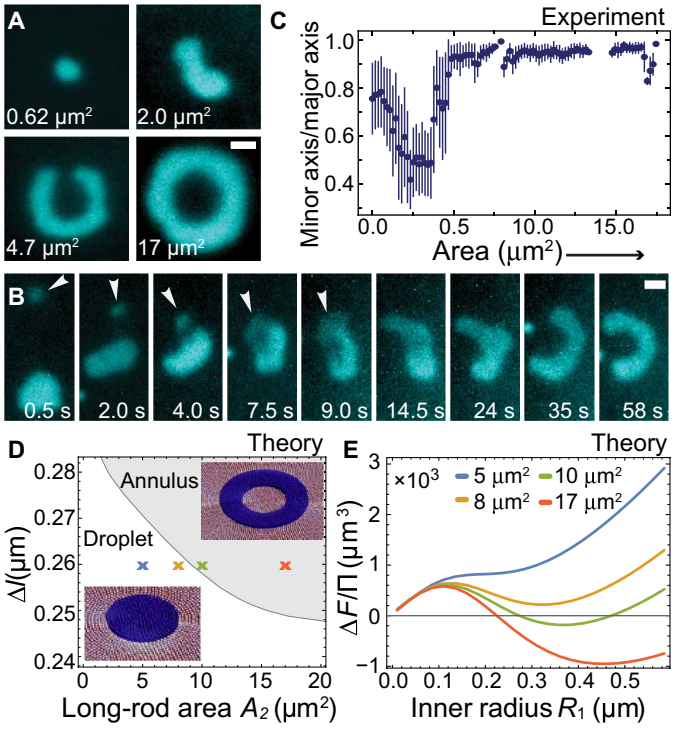

Fig. 5. Long-rod annular raft formation. (**A**) Increasing the area of a long-rod raft induces a shape transition from a circular droplet to elongated shapes before transforming into a horseshoe and eventually a complete annulus. (**B**) Two long-rod droplets are fused with an optical trap. Subsequently, the droplet transforms into a horseshoe shape. Arrow indicates the trap position. (**C**) The ratio of minor to major axis as a function of the raft area. Error bars represent SD of the average minor axis–to–major axis ratio for each area bin. (**D**) Theoretical prediction for the phase diagram of long-rod raft shapes as a function of raft area and the length difference between two rod species. A length difference of 0.26 μm corresponds to the experimental parameters. (**E**) Long-raft free energy landscape as a function of droplet radii/annulus inner radii for increasing raft size. Line colors correspond to the marked locations in the phase diagram in (D). The minima show the preferred droplet or annulus size. Scale bars, 1 μm.

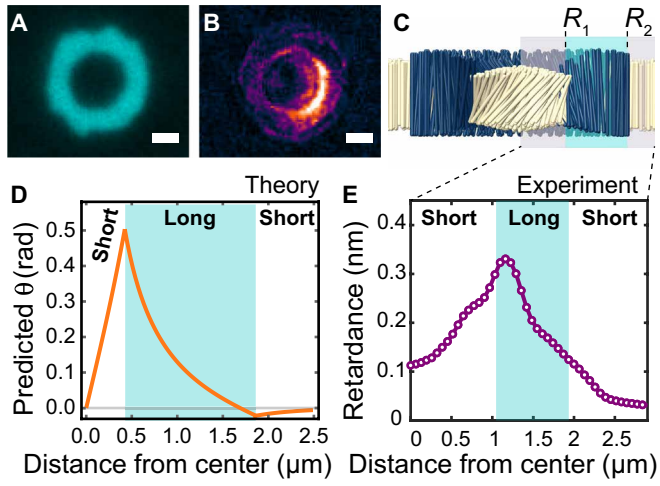

Fig. 6. Structure of annular long-rod rafts. (**A** and **B**) Fluorescence and LC-PolScope images of an annular long-rod raft. (**C**) Schematic of long-rod annulus. (**D**) Theoretical predictions for the radial rod twist exhibit a maximum at the inner edge and weak twist in the opposite direction at the outer edge. The annular width is highlighted in cyan. (**E**) Radially averaged retardance shows a peak in retardance at the inner edge, which decays into the membrane background. The annulus width as measured using fluorescence is highlighted in cyan. Scale bars, 1 μm.

droplets, the spontaneous curvature is determined by the properties of the phase-separated fluids, while in 3D vesicles, the curvature is selected by the structural asymmetry of the lipid bilayer itself.

We focused on the regime of comparable lengths where the tilt stiffness is positive $[\chi^{-1}(R) > 0]$ for all raft sizes, such that the edge twist only arises due to chiral asymmetry in the mixture (i.e., when $\Delta q \neq 0$). However, we anticipate that above a critical length difference, the edge-compression mechanism could also lead to negative twist stiffness $[\chi^{-1}(R) < 0]$ for a range of intermediate raft sizes. In such a regime, edges would spontaneously twist even in the absence of chirality. Furthermore, for sufficiently small chiral bias, negative twist stiffness should give rise to metastable rafts with twist that is opposite of the native one. Intriguingly, such counter-twisted rafts have been observed in membranes with a low net chirality (*22*). Furthermore, initial observations indicate that raft twist in fully achiral membranes is comparable or greater than in the chiral membrane (fig. S1).

While here we focused on the specific case of colloidal monolayers, the mechanism that generates spontaneous curvature can be recast as a generic consequence of the coupling between the compositional and orientational degrees of freedom, which should be relevant for all phase-separated fluid membranes with tilt degrees of freedom. These effects may be relevant to the broader class of fluid membrane systems, leading to a rich variety of 2D fluid domain shape equilibria.

More broadly, recent efforts that have uncovered multiple mechanisms can lead to assembly of finite-sized fluid assemblages. For example, surfactants and other amphiphilic molecules assemble into micelles and other finite-sized structures, but in these systems, the final assemblage size is always comparable to the size of the molecular constituents (*34*). A closely related class of cluster-forming systems, exemplified by magnetic fluids, is based on microscopic units with repulsive interactions whose range is much longer than the particle size. Such systems can form droplets with complex shapes, but, again, the cluster size is determined by the range of the repulsive potential, which is much larger than the constituent elements (*35*, *36*). An alternate self-closing mechanism that leads to finite-sized assemblages is exemplified by virus capsids, wherein a predetermined curvature emerges from the interactions of the microscopic building blocks, and the final assemblage size is determined by this curvature (*37*). A final mechanism is based on geometrical frustration, in which the finite size is determined by the fundamental incompatibility between local interactions and the global assembly constraints (*38*). Previous work demonstrated that assembly of colloidal rafts, which typically contain tens of thousands of rod-like molecules and are thus much larger than any molecular parameter, belongs to the last class of geometrically frustrated assemblages. In particular, modeling suggested that raft size was determined by the inherent frustration between the local preference of rods to twist and the incompatible global constraints of 2D sheet assembly that expel twist (*17*, *18*). However, the work described here demonstrates the presence of an additional previously unidentified self-closing mechanism, wherein the geometrical properties of the demixed fluid phases in length-asymmetric

molecules choose a preferred edge curvature, which, in turn, selects and stabilizes finite-sized assemblages.

MATERIALS AND METHODS

Experimental design

We used filamentous phages M13KO7 and *fd*. Both have ~7-nm diameter and a 2.8-μm persistence length. M13KO7 is 1200 nm long, and *fd* is 880 nm long (*19*). We also used the above phages with a single amino acid mutation in the major coat protein denoted as Y21M. This mutation yielded phages with opposite right-handed twist and an increased persistence length of 9.9 μm. All viruses were grown in liquid bacteria cultures and purified through multiple rounds of centrifugation, following previously established protocols (*39*). To eliminate the presence of longer multimers, the virus was prepared at isotropic-nematic coexistence concentrations, and only the isotropic phase was used for assembly of colloidal membranes as described elsewhere (*14*). Virus monodispersity was verified through gel electrophoresis.

All samples were prepared in 20 mM tris HCl, 100 mM NaCl (pH 8.0) (buffer). In the presence of depleting polymer (500-kDa Dextran), the viruses formed colloidal membranes, which were observed in sealed flow chambers that were prepared with ~100-μm-thick spacers. The chamber's top and bottom surfaces were coated with an acrylamide brush to prevent membrane adhesion (*40*). We labeled M13KO7 with fluorescent dye (DyLight 550 NHS ester for long-rod raft experiments and DyLight 488 NHS ester dye for short-rod raft experiments) with about 200 dye molecules per virus (*41*). Short-rod rafts were assembled in a mixture of 18% *fd*-Y21M and 82% M13KO7 (*19*). Long-rod rafts were studied in a mixture of 13% M13KO7 and 87% *fd*-Y21M at ~33 mg/ml dextran.

Previous experiments found that colloidal rafts were highly monodisperse (*19*). Increasing the dextran concentration from 40.0 to 40.5 mg/ml yielded polydisperse rafts, which were stable over weeks without disrupting the edge twist. For the measurements of retardance as a function of radius, the short-rod raft samples were assembled at 40.5 mg/ml dextran concentration.

For short-rod rafts, the chirality of the background membrane was adjusted by mixing the left-handed M13KO7 with the right-handed M13KO7-Y21M (*30*). A mixture of 37% M13KO7 and 63% M13KO7-Y21M shows no evidence of spontaneous twist (*22*). We define $\phi_{BG} = \frac{n_{M13KO7} - 0.37}{0.63}$ where $n_{M13KO7} = \frac{N_{M13KO7}}{N_{M13KO7} + N_{M13KO7\ Y21M}}$. $\phi_{BG} = 0$ corresponds to an achiral background membrane, and $\phi_{BG} = 1$ corresponds to maximally left-handed samples. Similarly, we define $\phi_{RFT} = \frac{0.26 - n_{fdwt}}{0.74}$, where $n_{fdwt} = \frac{N_{fdwt}}{N_{fdwt} + N_{fd\ Y21M}}$, so that $\phi_{Rft} = -1.0$ corresponds to maximally right-handed samples (*30*). To examine the influence of membrane chirality, we studied background membranes with ϕ_{BG}= 0.0, 0.4, and 1.0 while fixing $\phi_{RFT} = -1.0$. We also studied the case in which both the membrane chirality and the raft chirality were minimized, $\phi_{BG} = 0.0$ and $\phi_{RFT} = 0.0$.

Optical microscopy methods

Colloidal membranes were studied using a combination of differential interference contrast, phase contrast, and fluorescence microscopy. We used an inverted microscope (Nikon Eclipse TE2000-U) equipped with an oil immersion objective [Plan Fluor, 1.3 numerical aperture (NA) 100×]. For fluorescence microscopy, we used Semrock FITC (fluorescein isothiocyanate) and TRITC (tetramethylrhodamine isothiocyanate) filter cubes. For fluorescence excitation, we used the Lumencor SOLA light engine. Images were recorded with a scientific complementary metal-oxide semiconductor camera (Neo, Andor) that was controlled by the Micro-Manager software. The local membrane tilt was measured using LC-PolScope (*27*). LC-PolScope yields images in which the pixel intensity is proportional to local sample retardance. For a flat membrane in the image plane, it is possible to translate retardance into local rod tilt, as described elsewhere (*28*).

To quantify the shape dependence of long-rod rafts on their sizes, we systematically increased raft size by merging together multiple smaller rafts with optical tweezers. In comparison to short-rod rafts, which are repelled away from a trap (*19*, *22*), long-rod rafts could be directly trapped with a focused beam. We used a time-shared optical tweezers based on an acousto-optic deflector (AOD). The traps were controlled with custom LabView software, while the imaging and microscopy were controlled with the Micro-Manager software. Upon merging two droplets, the resulting shape fluctuations were recorded over several minutes. We repeated the merging process several times to capture the entire transition from a roughly circular droplet to an annulus. We repeated the transition multiple times across different samples and found that the shape dependence on long-rod domain size was consistent across all runs and independent of the microscopy observation techniques.

Data analysis

For all quantitative LC-PolScope measurements, we tracked rafts in MATLAB using standard particle tracking techniques (*42*). The radial retardance profile of each short-rod raft was first radially and then temporally averaged to minimize noise. Subsequently, the average background level retardance was subtracted. We measured the retardance of more than 30 rafts of various sizes. The averaged retardance maxima were then binned by raft radius, and the average value of each bin was plotted. Subsequently, the measurements were repeated for different background membrane compositions to determine the dependence of raft tilt on different background and raft chiralities. The low retardance of long-rod rafts made particle tracking from the retardance images impossible. The LC-PolScope imaging system calculates the local sample retardance from five images with different liquid crystal polarizer settings, including one in which the polarizer settings minimize the image intensity (*27*). In this image, a weak fluorescence signal is visible for the labeled long-rod rafts. We tracked the rafts in these max extinction images and measured the retardance at those positions in each calculated image.

We used Python and OpenCV to analyze the dependence of the long-rod domain shape on domain area. We set a binary intensity threshold to distinguish the fluorescently labeled long-rod domain from the membrane background. We found the contour of the domain in the binary image and calculated the area within the contour. Using OpenCV's "minAreaRect" function to find the minimum bounding rectangle for each maximum contour, we measured the short and long sides of the bounding rectangle as the minor and major axes of the domain. To quantify the degree of circularity of each merging domain, we calculated the ratio of the minor axis to the major axis. A ratio of 1 indicates a square bounding rectangle and, thus, a circular shape, while a smaller ratio indicates an elongated shape. The main contour area and minor axis–to–major axis ratio were calculated for each image. We then plotted the ratios as a

function of the areas of the long-rod domains and binned the data to see the resulting trends more clearly.

SUPPLEMENTARY MATERIALS

Supplementary material for this article is available at http://advances.sciencemag.org/cgi/content/full/6/31/eaba2331/DC1

REFERENCES AND NOTES

1. M. Goulian, R. Bruinsma, P. Pincus, Long-range forces in heterogeneous fluid membranes. *EPL* **22**, 145–150 (1993).
2. K. Kim, J. Neu, G. Oster, Curvature-mediated interactions between membrane proteins. *Biophys. J.* **75**, 2274–2291 (1998).
3. B. J. Reynwar, G. Illya, V. A. Harmandaris, M. M. Müller, K. Kremer, M. Deserno, Aggregation and vesiculation of membrane proteins by curvature-mediated interactions. *Nature* **447**, 461–464 (2007).
4. T. S. Ursell, W. S. Klug, R. Phillips, Morphology and interaction between lipid domains. *Proc. Natl. Acad. Sci. U.S.A.* **106**, 13301–13306 (2009).
5. S. L. Veatch, S. L. Keller, Separation of liquid phases in giant vesicles of ternary mixtures of phospholipids and cholesterol. *Biophys. J.* **85**, 3074–3083 (2003).
6. T. Baumgart, S. T. Hess, W. W. Webb, Imaging coexisting fluid domains in biomembrane models coupling curvature and line tension. *Nature* **425**, 821–824 (2003).
7. B. Palmieri, T. Yamamoto, R. C. Brewster, S. A. Safran, Line active molecules promote inhomogeneous structures in membranes: Theory, simulations and experiments. *Adv. Colloid Interface Sci.* **208**, 58–65 (2014).
8. D. Brown, E. London, Functions of lipid rafts in biological membranes. *Annu. Rev. Cell Dev. Biol.* **14**, 111–136 (1998).
9. K. Simons, W. L. Vaz, Model systems, lipid rafts, and cell membranes. *Annu. Rev. Biophys. Biomol. Struct.* **33**, 269–295 (2004).
10. S. Meinhardt, R. L. Vink, F. Schmid, Monolayer curvature stabilizes nanoscale raft domains in mixed lipid bilayers. *Proc. Natl. Acad. Sci. U.S.A.* **110**, 4476–4481 (2013).
11. R. M. Weis, H. M. McConnell, Two-dimensional chiral crystals of phospholipid. *Nature* **310**, 47–49 (1984).
12. V. M. Kaganer, H. Möhwald, P. Dutta, Structure and phase transitions in Langmuir monolayers. *Rev. Mod. Phys.* **71**, 779–819 (1999).
13. H. M. McConnell, A. Radhakrishnan, Condensed complexes of cholesterol and phospholipids. *Biochim. Biophys. Acta* **1610**, 159–173 (2003).
14. E. Barry, Z. Dogic, Entropy driven self-assembly of nonamphiphilic colloidal membranes. *Proc. Natl. Acad. Sci. U.S.A.* **107**, 10348–10353 (2010).
15. Y. Yang, E. Barry, Z. Dogic, M. F. Hagan, Self-assembly of 2D membranes from mixtures of hard rods and depleting polymers. *Soft Matter* **8**, 707–714 (2012).
16. L. Kang, T. Gibaud, Z. Dogic, T. C. Lubensky, Entropic forces stabilize diverse emergent structures in colloidal membranes. *Soft Matter* **12**, 386–401 (2016).
17. L. Kang, T. C. Lubensky, Chiral twist drives raft formation and organization in membranes composed of rod-like particles. *Proc. Natl. Acad. Sci. U.S.A.* **114**, E19–E27 (2017).
18. R. Sakhardande, S. Stanojeviea, A. Baskaran, A. Baskaran, M. F. Hagan, B. Chakraborty, Theory of microphase separation in bidisperse chiral membranes. *Phys. Rev. E* **96**, 012704 (2017).
19. P. Sharma, A. Ward, T. Gibaud, M. F. Hagan, Z. Dogic, Hierarchical organization of chiral rafts in colloidal membranes. *Nature* **513**, 77–80 (2014).
20. J. V. Selinger, Interpretation of saddle-splay and the Oseen-Frank free energy in liquid crystals. *Liquid Crystals Reviews* **6**, 129–142 (2018).
21. N. Chaturvedi, R. D. Kamien, Gnomonious projections for bend-free textures: thoughts on the splay-twist phase. *Proc. Math. Phys. Eng. Sci.* **476**, 20190824 (2020).
22. J. M. Miller, C. Joshi, P. Sharma, A. Baskaran, A. Baskaran, G. M. Grason, M. F. Hagan, Z. Dogic, Conformational switching of chiral colloidal rafts regulates raft–raft attractions and repulsions. *Proc. Natl. Acad. Sci. U.S.A.* **116**, 15792–15801 (2019).
23. U. Seifert, Configurations of fluid membranes and vesicles. *Adv. Phys.* **46**, 13–137 (1997).
24. R. B. Meyer, A. Ciferri, W. R. Krigbaum, *Polymer Liquid Crystals* (Academic Press Incorporated, 1982).
25. P. De Gennes, Polymeric liquid crystals: Frank elasticity and light scattering. *Mol. Cryst. Liquid Cryst.* **34**, 177–182 (1976).
26. D. W. Atkinson, C. Santangelo, G. M. Grason, Constant spacing in filament bundles. *New J. Phys.* **21**, 062001 (2019).
27. R. Oldenbourg, G. Mei, New polarized-light microscope with precision universal compensator. *J. Microsc.* **180**, 140–147 (1995).
28. E. Barry, Z. Dogic, R. B. Meyer, R. A. Pelcovits, R. Oldenbourg, Direct measurement of the twist penetration length in a single smectic A layer of colloidal virus particles. *J. Phys. Chem. B* **113**, 3910–3913 (2009).
29. P. G. de Gennes, J. Prost, *The Physics of Liquid Crystals*, in International Series of Monographs on Physics (Oxford Univ. Press, Oxford, ed. 2, 1995), vol. 83, pp. 601.
30. T. Gibaud, C. N. Kaplan, P. Sharma, M. J. Zakhary, A. Ward, R. Oldenbourg, R. B. Meyer, R. D. Kamien, T. R. Powers, Z. Dogic, Achiral symmetry breaking and positive Gaussian modulus lead to scalloped colloidal membranes. *Proc. Natl. Acad. Sci. U.S.A.* **114**, E3376–E3384 (2017).
31. T. Gibaud, E. Barry, M. J. Zakhary, M. Henglin, A. Ward, Y. Yang, C. Berciu, R. Oldenbourg, M. F. Hagan, D. Nicastro, Reconfigurable self-assembly through chiral control of interfacial tension. *Nature* **481**, 348–351 (2012).
32. L. L. Jia, M. J. Zakhary, Z. Dogic, R. A. Pelcovits, T. R. Powers, Chiral edge fluctuations of colloidal membranes. *Physical Review E* **95**, 060701 (2017).
33. H. Hotani, Transformation pathways of liposomes. *J. Mol. Biol.* **178**, 113–120 (1984).
34. S. Safran, *Statistical Thermodynamics of Surfaces, Interfaces, and Membranes* (CRC Press, 2018).
35. A. J. Dickstein, S. Erramilli, R. E. Goldstein, D. P. Jackson, S. A. Langer, Labyrinthine pattern formation in magnetic fluids. *Science* **261**, 1012–1015 (1993).
36. M. Seul, D. Andelman, Domain shapes and patterns: The phenomenology of modulated phases. *Science* **267**, 476–483 (1995).
37. J. D. Perlmutter, M. F. Hagan, Mechanisms of virus assembly. *Annu. Rev. Phys. Chem.* **66**, 217–239 (2015).
38. G. M. Grason, Perspective: Geometrically frustrated assemblies. *J. Chem. Phys.* **145**, 110901 (2016).
39. T. Maniatis, J. Sambrook, E. Fritsch, *Molecular Cloning: A Laboratory Manual*, (Cold Spring Harbor Laboratory, Cold Spring Harbor, 1989).
40. A. Lau, A. Prasad, Z. Dogic, Condensation of isolated semi-flexible filaments driven by depletion interactions. *EPL* **87**, 48006 (2009).
41. M. P. Lettinga, E. Barry, Z. Dogic, Self-diffusion of rod-like viruses in the nematic phase. *EPL* **71**, 692–698 (2005).
42. J. C. Crocker, D. G. Grier, Methods of digital video microscopy for colloidal studies. *J. Colloid Interf. Sci.* **179**, 298–310 (1996).
43. S. Asakura, F. Oosawa, On interaction between two bodies immersed in a solution of macromolecules. *J. Chem. Phys.* **22**, 1255–1256 (1954).
44. G. M. Grason, Colloquium: Geometry and optimal packing of twisted columns and filaments. *Rev. Mod. Phys.* **87**, 401–419 (2015).
45. A. Panaitescu, G. M. Grason, A. Kudrolli, Measuring geometric frustration in twisted inextensible filament bundles. *Phys. Rev. E* **95**, 052503 (2017).

Acknowledgments: We are grateful to acknowledge the helpful discussion with C. Joshi regarding the theoretical aspects of this work. **Funding:** This work was primarily supported by NSF–Materials Research Science and Engineering Centers (MRSEC)–2011486 (to M.F.H. and Z.D.). We also acknowledge support of NSF–Division of Materials Research (DMR)-–1905484 (to Z.D.) and NSF-DMR-1608862 (to G.M.G.) and use of the Brandeis MRSEC optical microscopy and biosynthesis facility supported by NSF-MRSEC-1420382. **Author contributions:** J.M.M., D.H., G.M.G., and Z.D. designed the research; J.M.M., J.R., and D.H. performed the research; P.S. acquired preliminary data; J.M.M., D.H., and J.R. analyzed the data; and J.M.M., D.H., J.R., M.F.H., G.M.G., and Z.D. wrote the paper. **Competing interests:** The authors declare that they have no competing interests. **Data and materials availability:** All data needed to evaluate the conclusions in the paper are present in the paper and/or the Supplementary Materials. Additional data and/or Mathematica codes used to evaluate model predictions may be requested from the authors.

Submitted 15 November 2019
Accepted 16 June 2020
Published 29 July 2020
10.1126/sciadv.aba2331

Citation: J. M. Miller, D. Hall, J. Robaszewski, P. Sharma, M. F. Hagan, G. M. Grason, Z. Dogic, All twist and no bend makes raft edges splay: Spontaneous curvature of domain edges in colloidal membranes. *Sci. Adv.* **6**, eaba2331 (2020).